PAPER • OPEN ACCESS

Ultrafast multidimensional spectroscopy with field resolution and noncollinear geometry at mid-infrared frequencies

To cite this article: Thomas Deckert *et al* 2022 *New J. Phys.* **24** 023005

New Journal of Physics
The open access journal at the forefront of physics

Deutsche Physikalische Gesellschaft DPG
IOP Institute of Physics

Published in partnership with: Deutsche Physikalische Gesellschaft and the Institute of Physics

OPEN ACCESS

RECEIVED
6 October 2021

REVISED
22 December 2021

ACCEPTED FOR PUBLICATION
11 January 2022

PUBLISHED
7 February 2022

PAPER

Ultrafast multidimensional spectroscopy with field resolution and noncollinear geometry at mid-infrared frequencies

Thomas Deckert[1,4], **Jonas Allerbeck**[1,2,4], **Takayuki Kurihara**[3] and **Daniele Brida**[1,*]

[1] Department of Physics and Materials Science, Université du Luxembourg, 162a Avenue de la Faïencerie, 1511 Luxembourg, Luxembourg
[2] Nanotech@surfaces Laboratory, Empa - Swiss Federal Laboratories for Materials Science and Technology, Überlandstrasse 129, 8600 Dübendorf, Switzerland
[3] Institute for Solid State Physics, The University of Tokyo, 277-8581, 5-1-5 Kashiwanoha, Kashiwa, Chiba, Japan
[4] These authors equally contributed to the work.
[*] Author to whom any correspondence should be addressed.

E-mail: daniele.brida@uni.lu

Keywords: two-dimensional spectroscopy, four-wave mixing, terahertz spectroscopy, electro-optic sampling

Abstract

Energetic correlations and their dynamics govern the fundamental properties of condensed matter materials. Ultrafast multidimensional spectroscopy in the mid infrared is an advanced technique to study such coherent low-energy dynamics. The intrinsic many-body phenomena in functional solid-state materials, in particular few-layer samples, remain widely unexplored to this date, because complex and weak sample responses demand versatile and sensitive detection. Here, we present a novel setup for ultrafast multidimensional spectroscopy with noncollinear geometry and complete field resolution in the 15–40 THz range. Electric fields up to few-100 kV cm^{-1} drive coherent dynamics in a perturbative regime, and an advanced modulation scheme allows to detect nonlinear signals down to a few tens of V cm^{-1} entirely background-free with high sensitivity and full control over the geometric phase-matching conditions. Our system aims at the investigation of correlations and many-body interactions in condensed matter systems at low energy. Benchmark measurements on bulk indium antimonide reveal a strong six-wave mixing signal and map ultrafast changes of the band structure with access to amplitude and phase information. Our results pave the way towards the investigation of functional thin film materials and few-layer samples.

1. Introduction

Ultrafast multidimensional spectroscopy in the mid infrared has become an established technique to study molecular systems with discrete resonances and energy levels [1–3]. In contrast to standard pump-probe spectroscopy, the spectral interference of two pump pulses imprints a unique modulation on the sample response and expands a conventional pump-probe spectrum by an excitation frequency axis [4].

With recent developments of ultrafast pulse sources, increased attention shifted to solid state materials, where the mid-infrared (mid-IR) pulses drive and excite the motions of free electrons, the vibrations of crystal lattices, and the precessions of spins [5]. Continuous energy bands and collective many-body excitations must be probed with femtosecond (fs) time resolution, increasing the experimental complexity compared to molecular systems with discrete energy levels. Previous studies have shown promising results, including coherent low energy dynamics, of the semiconductor indium antimonide (InSb) [6, 7] by observing two phonon quantum coherences [8], intersubband excitations of electrons in semiconductor quantum wells [9, 10] and their interaction with longitudinal optical phonons [11, 12], carrier dynamics of graphene in the non-perturbative limit [12], the response of collective spin waves in antiferromagnetic crystals [13], and disordered electron systems observing a marginal Fermi glass [14]. Beyond this, mid-IR two-dimensional (2D) spectroscopy shows high potential to study low-temperature phases in correlated materials such as copper oxides, accessing fundamental decoherence processes of excited states [15].

Especially layered materials are an interesting platform to be explored in their two-dimensional limit, where conventional pump-probe spectroscopy is already well established [16, 17]. In all multidimensional studies mentioned above [6–8, 10–14], the electric field is fully resolved in the time-domain by means of electro-optic sampling (EOS). Especially, the phase is a precious information, yet still overlooked in the majority of 2D spectroscopy studies. It is inaccessible to time-integrated readout schemes unless the local oscillator is fully characterized in amplitude and phase before being superimposed to the sample response [18–20].

Dynamic changes in the optical response of semiconductors with excitation in the perturbative regime are typically on the order of a few percent in bulk samples [21] and several orders of magnitude below that for thin films or 2D materials [16], which imposes several requirements on an experimental system: (i) high sensitivity also at low fluence [15], (ii) electric peak fields in the kV cm^{-1} to MV cm^{-1} range, and (iii) femtosecond (fs) temporal resolution [15]. Although recent advances in terahertz pulsed laser sources have led to significant improvements, pulsed radiation with high electric fields usually cannot offer sufficient counting statistics in order to improve the signal to noise ratio in experiments. In addition, 2D experiments with collinear or partially collinear geometries measure the nonlinear signal superimposed by driving electric fields and cannot offer full control of phase matching, which requires significant post-processing of the data [22].

In this work, we overcome these limitations by combining multi-cycle pulses with peak electric fields of few-100 kV cm^{-1}, an efficient time-domain field sampling technique, and noncollinear geometry. We present a novel setup for ultrafast coherent spectroscopy with high sensitivity that allows to resolve nonlinear signals with field amplitudes down to a few tens of V cm^{-1}. The experimental geometry enables full control of phase matching, efficient spatial filtering and background-free signal detection, based on a double-pulse modulation and multi-demodulator readout. We achieve high stability of the system over multiple hours of operation without active phase stabilization. Finally, to benchmark the experimental setup, we performed measurements on a bulk InSb sample and compare them to complementary literature [6–8] revealing ultrafast changes of the bandgap that are a superposition of transient renormalization, the Franz–Keldysh effect, and non-uniform absorption. We demonstrate the advantages of field resolution by analyzing also the spectral phase in the framework of 2D spectroscopy.

2. Noncollinear multidimensional spectroscopy with field resolution

2.1. Generation of phase-locked mid-infrared pulses

The experimental setup presented in figure 1(a) is based on a ytterbium:KGW laser from Light Conversion Ltd operating at 50 kHz repetition rate and providing fundamental pulses at 1030 nm with 230 fs duration. Mid-IR pulses are generated via difference frequency generation (DFG) in gallium-(II)-selenide (GaSe) between the fundamental of the laser and the output of a near-infrared noncollinear optical parametric amplifier at 1.1–1.2 μm. This method allows the generation of pulses between 7.5 μm and 30 μm (15–40 THz) [23]. In this experiment, we employ multi-cycle pulses between 20 and 30 THz that are generated by a 1.2 mm-thick GaSe crystal and feature up to 120 nJ pulse energy, 2–3 THz bandwidth, and 450 fs full-width-at-half-maximum duration, as depicted by the intensity spectra in figure 1(b). This configuration efficiently achieves high peak electric fields to drive nonlinear processes. Thinner crystals enable the generation of shorter pulses with duration below 70 fs and similar peak electric field in the same experiment [23].

2.2. Creation and detection of four pulse replicas in a box geometry

A compact Michelson-type interferometer splits initial mid-IR pulses into four identical replicas by three gold coated germanium beam splitters positioned near Brewster's angle at 76°. After the interferometer, the pulses follow parallel trajectories in a square box geometry with 12 mm separation (figure 1(c)). The two arms serving as pump pulses (#1 orange and #2 blue) are approximately twice as intense compared to the probe pulse (#3 green). A fourth reference pulse (purple) simplifies the experimental alignment and data acquisition, but is unused in the experiment since a local oscillator is not needed for the detection of the nonlinear signal. The probe pulse remains fixed in the absolute timeframe, while the relative delays between the pump replicas are controlled by motorized retroreflectors setting coherence time τ and pump-probe delay time T in the experiment. The complete time ordering with respect to the sampling axis t is depicted in figure 1(c): relative delays τ and T are defined positive when maintaining the logic pulse order (#1–#2–#3). The probe pulse center defines $t = 0$ ps. As illustrated by the inset, the coherence time τ can be scanned by moving either pump pulse #1 or #2.

A 90-degree off-axis parabolic mirror with effective focal length of 50 mm focusses all pulses to the sample achieving approximately 100 μm focal diameter. Nonlinear signals generated by pump and probe

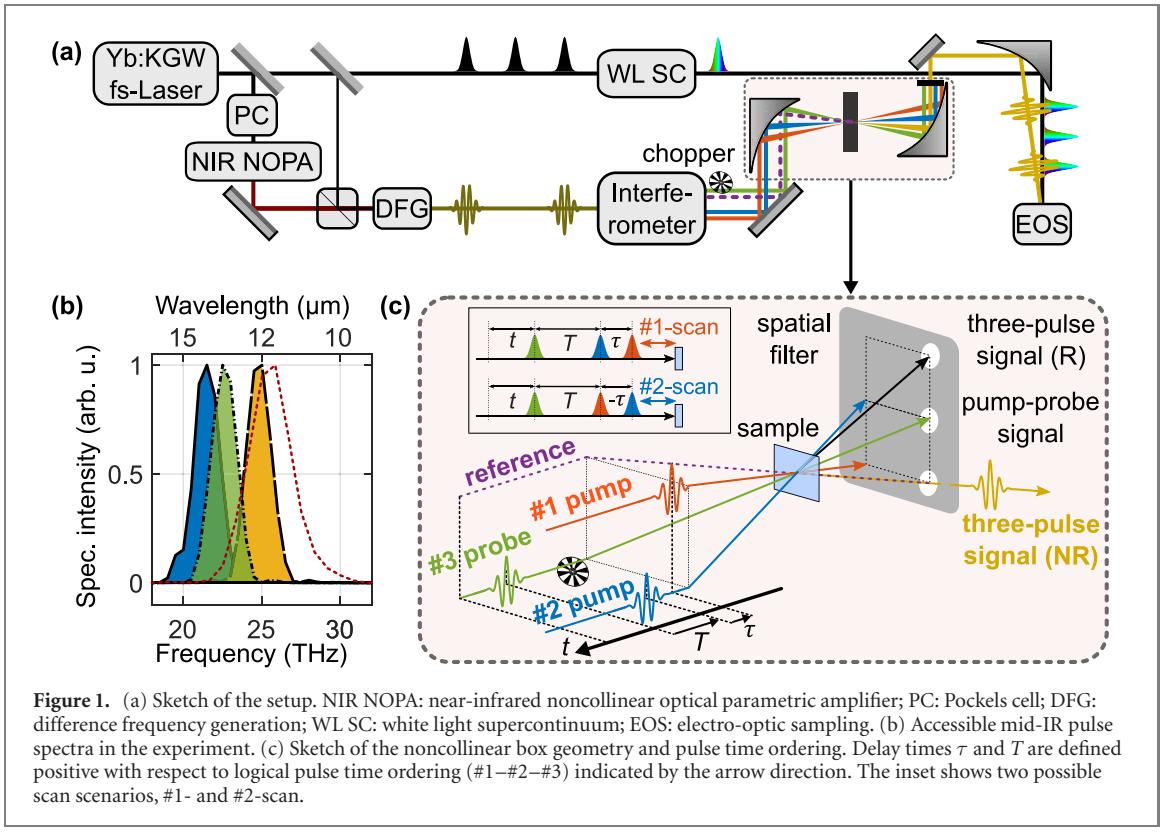

Figure 1. (a) Sketch of the setup. NIR NOPA: near-infrared noncollinear optical parametric amplifier; PC: Pockels cell; DFG: difference frequency generation; WL SC: white light supercontinuum; EOS: electro-optic sampling. (b) Accessible mid-IR pulse spectra in the experiment. (c) Sketch of the noncollinear box geometry and pulse time ordering. Delay times τ and T are defined positive with respect to logical pulse time ordering (#1–#2–#3) indicated by the arrow direction. The inset shows two possible scan scenarios, #1- and #2-scan.

pulse interaction are emitted in different spatial directions following wave vector conservation $\vec{k}_S = \sum_i \vec{k}_i$, where index i is the pulse number. This includes standard two-pulse pump-probe signals where $\vec{k}_S = \vec{k}_i - \vec{k}_i + \vec{k}_3$ and $i = 1, 2$, as well as non-rephasing (NR) $\vec{k}_S = \vec{k}_1 - \vec{k}_2 + \vec{k}_3$ and rephasing (R) $\vec{k}_S = -\vec{k}_1 + \vec{k}_2 + \vec{k}_3$ three-pulse signals. As indicated by figure 1(c), the NR signal is emitted into the fourth quadrant of the box geometry when assuming logical pulse ordering #1–#2–#3, and becomes the R signal for a #2–#1–#3 pulse ordering [22]. This signal emission can be equivalently explained as probe pulse diffraction from a transient grating created by the spatiotemporal interference of two pump pulses. The grating planes are perpendicular to the sample surface and oriented either horizontally, vertically, or diagonally depending on the k-vectors of excitation pulses [24–26]. Higher-order nonlinear signals emitted in other spatial directions are also measurable, but are not considered in the current experiment. After sample interaction, a second parabolic mirror recollimates all pulses and signals. The noncollinear geometry of the experiment enables precise spatial filtering and background-free detection of the emitted nonlinear signal of interest (yellow profile in figure 1(c)). EOS is performed in gallium selenide (thickness 70–80 μm) with an ultrashort white light supercontinuum that acts as the gating pulse. It is compressed to 14 fs with an SF10 prism pair (apex angle 61°, apex distance 140 mm) [23]. This approach enables phase-sensitive detection of the transmitted and generated signals with sub-optical-cycle precision thus allowing a temporal resolution much shorter than the temporal duration of the mid infrared pulses and allowing us to access the phase information.

2.3. Alignment procedure

We apply a sophisticated procedure to achieve space–time overlap of all four pulses on the sample. At first, we use a sensitive pyroelectric detector to align all four interferometer arms to the square-box geometry with appropriate apertures. This results in perfect 1:1 imaging of the beam geometry after both parabolic mirrors. A 100 μm pinhole is used for refining the spatial overlap at the sample position. Without spatial filtering all initial pulses are detected by EOS simultaneously. We adjust the temporal overlap with manual and motorized retroreflectors in the interferometer, and with respect to EOS time t. In a second step, the reference pulse, which is collinear to the expected Four-Wave Mixing (FWM) signal, allows to precisely optimize the EOS detection. A spatial filter (SF) after the collimating parabolic mirror blocks the three driving pulses and passes the FWM signal.

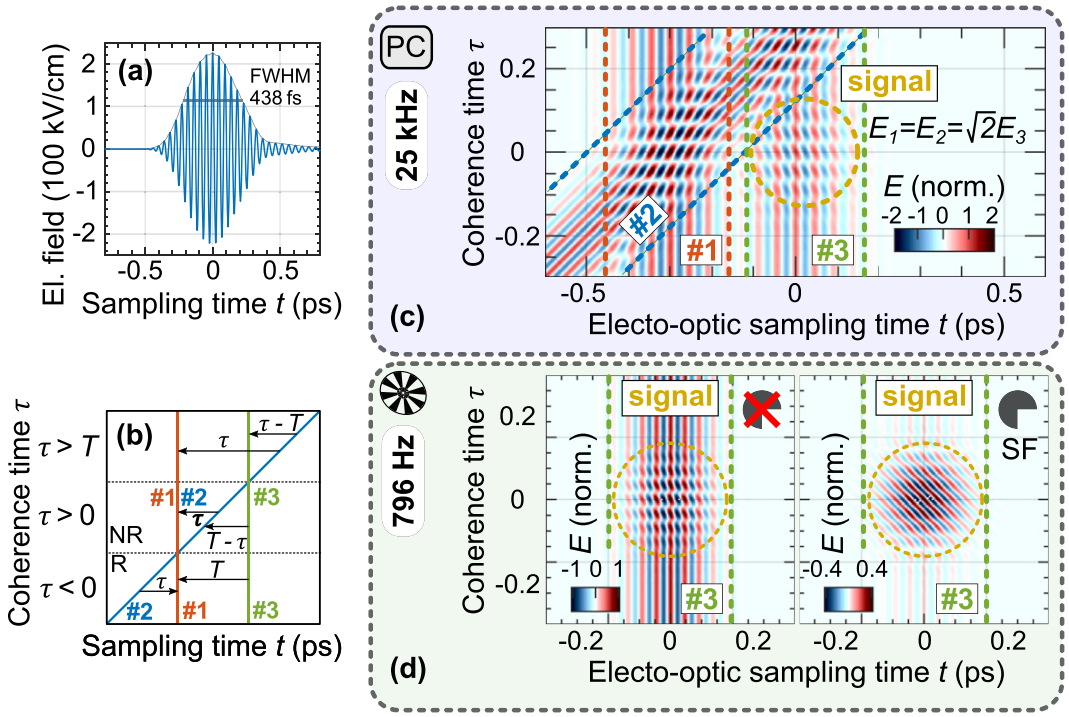

Figure 2. (a) Electric field profile of the reference pulse. (b) Pulse #2 scanning scheme in the experiment. Colored lines show the relative pulse positions at various coherence times τ. (c) Simulation of the measured electric field measured at 25 kHz PC demodulation frequency and without spatial filter (SF). The electric fields of pump and probe pulses, $E_{1,2}(t,\tau)$and $E_3(t,\tau)$ respectively, align according to panel (b). (d) Simulation of a FWM signal measured at 796 Hz chopper demodulation frequency without (left panel) and with (right panel) SF blocking both pump pulses and the probe pulse. A static background in the right panel is due to residual probe pulse scattering at the sample. Electric field amplitude in panels (c) and (d) is normalized with respect to $E_1(t,\tau)$.

3. Data acquisition and processing

3.1. Electro-optic sampling and pulse modulation

For efficient signal detection we employ double modulation and a fast-scan readout scheme based on continuous scanning of the EOS gate pulse [27]. As indicated in figure 1(a), a Pockels cell (PC) modulates the mid-IR pulses at the first laser subharmonic (25 kHz) enabling sensitive measurements of the electric field profiles of pulses from all interferometer arms [23]. Figure 2(a) shows the field profile of the reference pulse as a function of the sampling time. To discriminate nonlinear signals from pulse scattering that leaks through the SF, we introduce a second modulation only to the probe pulse inside the interferometer. A mechanical chopper is synchronized to the 64th subharmonic (796 Hz) of the laser repetition rate. Dual-channel lock-in demodulation allows simultaneous readout at both modulation frequencies.

3.2. Pulse scanning configuration

In a typical experiment, the coherence time τ between pump pulses is scanned for a series of pump-probe delay times T. For a precise understanding of the pulse scanning procedure and signal filtering we simulate the experiment. Figure 2(b) illustrates the pulse scanning configuration, showing rephasing (R) and NR signal contributions in lower and upper hemisphere respectively. For $\tau > 0$ ps, the effective delay time T^*, i.e. the difference between probe pulse and closest pump pulse, changes with τ: $T^* = T - \tau$ or $T^* = \tau - T$. Only in the lower hemisphere, for $\tau < 0$ ps and pulse ordering #2–#1–#3, T is well defined. We scan the delay of pump pulse #2 with respect to the fixed position of pump pulse #1, which is beneficial for geometrical reasons. The transient grating created by the interaction of fixed pulses #1 and #3 is orthogonal to the scanning pulse #2 and its diffraction is thus suppressed, such that no disturbing signals occur at short delay T, when #1 and #3 overlap.

Figure 2(c) shows the electric field profile of all interacting pulses as well as the FWM signal as detected at the PC modulation frequency. This simulation calculates the individual pulse contributions with instantaneous sample response, highlighting the precise filter mechanism for FWM signals in the experiment. It assumes a linear superposition of signals in the time domain, which each correspond to 2D Gaussian peaks in the frequency domain. Pulses are centered at 22 THz and the intensity of pump pulses is twice as high as of the probe to mimic the driving pulses in the experiment. The field amplitude is color

coded as a function of coherence and sampling time with fixed delay time $T = 0.3$ ps. Colored dashed lines in figure 2(c) indicate the temporal position of the pulses in accordance with figure 2(b). In addition to the pulses #1–#3, figure 2(c) shows an exemplary FWM signal (yellow circle) centered at $\tau = t = 0$ ps, which interferes with the probe pulse (#3 green).

Figure 2(d) shows the calculated signal obtained with demodulation at the chopper frequency (796 Hz), where left and right panels are obtained without and with a SF respectively. In this case only the linear probe pulse transmission and nonlinear signals that include interaction with the probe pules are detected. The SF eliminates the linear probe pulse contribution (#3 green), however, a residual linear background remains unavoidable in the experiment and is therefore also indicated in the simulation (right panel of figure 2(d)). This scattering contribution results from inhomogeneities of the sample and remains static in the experiment, allowing for complete removal in post processing.

3.3. Data processing in time and frequency domain

Mid-IR pulses generated via DFG are intrinsically phase-stable, however, interferometric instabilities between the near-infrared noncollinear optical parametric amplifier (NIR NOPA) and the fundamental cause minor carrier-envelope phase fluctuations on the order of few fs, which is well below the duration of one field cycle. Our advanced double-modulation technique and the weak scattering background allow to correlate successive field scans at individual time steps even if no nonlinear signal is present [27]. If scattering of pump and probe pulses through the SF is weak, the reference pulse can serve to set the phase of the signal. To avoid any influence with the nonlinear signal, we remove its spatial overlap with the other pulses on the sample. Nevertheless, owing to the compact interferometer design, phase fluctuations between mid-IR pulses remain negligible.

Coherence (excitation) and sampling (detection) frequency are retrieved via numeric fast Fourier transform and indicated by ν_τ and ν_t respectively. We apply a high-order Gaussian notch filter in the frequency domain to further enhance our signal and remove remaining static background signals at $\nu_\tau = 0$ that result from scattering or the reference pulse. Upon inverse Fourier transform we obtain a clean and background-free time-domain representation of the nonlinear signal.

In combination, the advanced data acquisition and post processing technique presented here allow to measure signals of only a few 10 V cm^{-1} completely background-free with extreme sensitivity. Full signal retrieval in the time domain enables the tracking of spectral dynamics with access to amplitude and phase. Spectra are phased with respect to the positive field maximum of the nonlinear signal at $t = \tau = 0$ ps, defining a constant phase offset. The high passive phase stability of the setup allows for consecutive data acquisition over several hours further enhancing the sensitivity to measure weak signals. Spatial filtering of high intensity driving pulses significantly reduces the absolute field amplitude in the detection crystals and hence reduces the influence of nonlinear effects that are inherent to collinear geometries.

4. High-order nonlinear spectroscopy with indium antimonide

4.1. High-order nonlinear spectroscopy signals in the time and frequency domain

Benchmark measurements of the semiconductor InSb demonstrate the capabilities of the experimental setup by tracking the ultrafast coherent response and charge-carrier dynamics of the system with significantly higher sensitivity compared to previous studies [6–8]. The 60 μm-thick bulk sample with $\langle 100 \rangle$-orientation is free-standing and optically polished on both sides. InSb has a direct bandgap of 0.18 eV (43.6 THz) at 300 K, located at the center of the Brillouin zone (Γ-point) and capturing all relevant photoexcitation channels at low energy [28]. Relevant optical phonon resonances lie between 4 and 6 THz thus remaining off-resonant to the frequencies accessed by the experiment. Our mid-IR pulses (figure 2(a)) excite carriers via two-photon absorption (TPA), enabling nonresonant penetration of the bulk sample and providing a large interaction length [29].

Figures 3(a)–(f) shows the emitted nonlinear three-pulse signal of InSb in the time (upper panels) and frequency (lower panels) domain measured in the direction of the reference pulse (purple) and after spatial filtering according to figure 1(c). From left to right, the panels show experimental data obtained at different pulse frequencies tuned between 21 and 25 THz. The pump-probe delay time T is between 100 and 200 fs. Colored dashed lines in time-domain plots map the pulse positions according to the scan configuration shown in figure 2(b). In the frequency domain, the black diagonal is a guide to the eye representing equal excitation and detection energy. The vertical and horizontal dashed lines show the center frequency of the driving pulses. As a result of the strong optical fields, the center of gravity of 2D spectra shifts along the vertical as indicated by red and blue arrows and discussed in the following.

The origin of the nonlinear signals in figure 3 can be understood by linear scattering from a transient population grating induced by TPA. Hereby, the spatial and temporal interference of pump pulses induces a

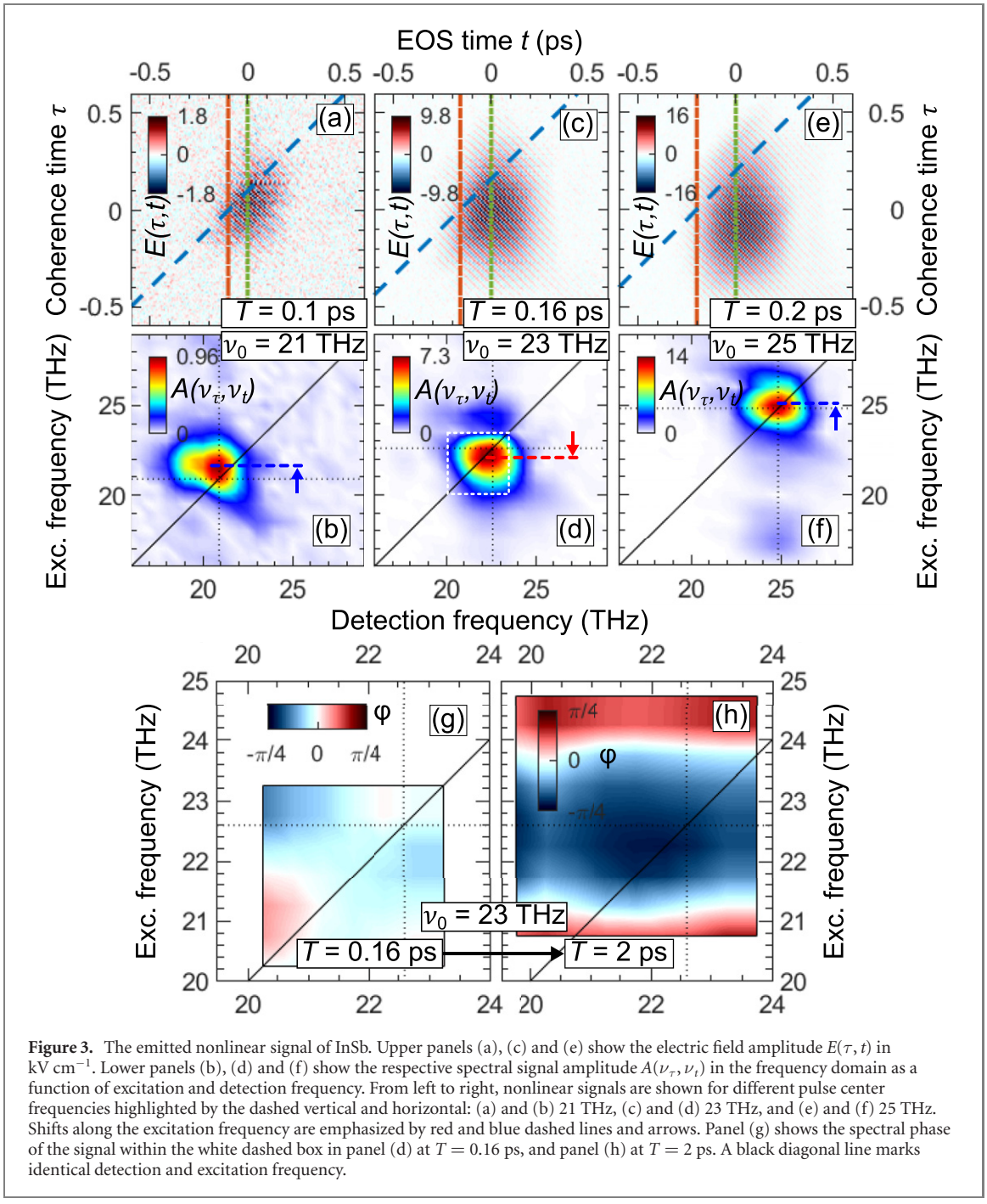

Figure 3. The emitted nonlinear signal of InSb. Upper panels (a), (c) and (e) show the electric field amplitude $E(\tau, t)$ in kV cm^{-1}. Lower panels (b), (d) and (f) show the respective spectral signal amplitude $A(\nu_\tau, \nu_t)$ in the frequency domain as a function of excitation and detection frequency. From left to right, nonlinear signals are shown for different pulse center frequencies highlighted by the dashed vertical and horizontal: (a) and (b) 21 THz, (c) and (d) 23 THz, and (e) and (f) 25 THz. Shifts along the excitation frequency are emphasized by red and blue dashed lines and arrows. Panel (g) shows the spectral phase of the signal within the white dashed box in panel (d) at $T = 0.16$ ps, and panel (h) at $T = 2$ ps. A black diagonal line marks identical detection and excitation frequency.

strongly nonlinear modulation of the dielectric function that diffracts the probe pulse into the direction of detection [24–26, 30, 31]. Charge carrier relaxation and carrier diffusion in InSb, seen as amplitude reduction in the 2D experiments, is orders of magnitude slower compared to ultrafast processes studied in this work and does not contribute to the observed dynamics [32–36]. The nonlinear signals contain a variety of meaningful information, including: (i) time domain modulations [6–8], (ii) spectral line shape dynamics such as asymmetries, shifts and distortions, (iii) analysis of spectral phase or real- and imaginary amplitude in the frequency domain. With precise control of the pump-probe delay T we can investigate the evolution of these dynamics with fs time resolution. In addition, the flexibility of scanning the fundamental mid-IR pulse frequency as shown in figure 3 can distinguish excitation energy dynamics across a wide range.

Figure 3(g) maps the spectral phase in the window indicated by the white dashed box in figure 3(d), where the amplitude of the signal is sufficiently high for an accurate definition of phase. For comparison we also show the phase information for a larger delay $T = 2$ ps (figure 3(h)). Linear phase contributions, which are introduced arbitrarily with respect to the zero-time definition $t = \tau = 0$ ps, are removed along the excitation and detection frequency independently to highlight the nonlinear components of the phase.

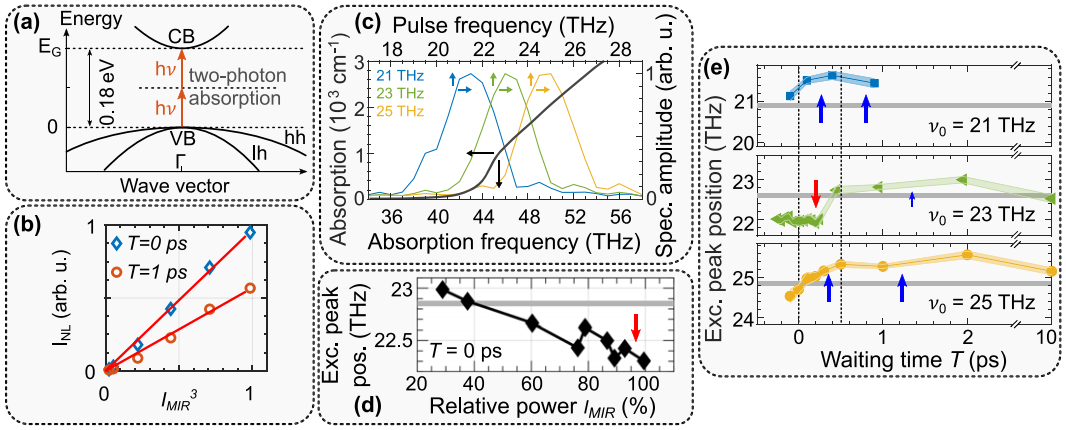

Figure 4. (a) Schematic illustration of the unperturbed band structure of InSb near the Γ-point. TPA at 90 meV (23 THz) efficiently drives interband transitions. VB: valence band, CB: conduction band, lh: light hole, hh: heavy hole. (b) Cubic power dependence of the integrated nonlinear signal I_{NL} as a function of the total MIR intensity I_{MIR} (pump and probe pulses) at two different waiting times. (c) Mid-IR amplitude spectra used in the four-wave mixing experiments. Linear absorption of InSb (left and bottom axes) reproduced from reference [42] with original data from [43, 44]. Note that top and bottom frequency axis are scaled with factor two to highlight TPA. (d) Power dependence of the excitation peak position for waiting time $T = 0$ ps with respect to the center frequency of driving pulses (grey line). (e) Temporal evolution of the excitation peak position extracted from 2D frequency maps for pulse center frequencies (grey line) at 21, 23, and 25 THz (top to bottom). The shaded areas highlight the fit uncertainty.

Figure 3(g) shows only a small nonlinear phase, whose variations from a constant value likely originate from the asymmetric time-domain signal profile in figure 3(c) owing to the delayed transient grating built-up when $\tau > 0$ ps and $t < 0$ ps. At longer delays, the spectral phase is constant along the detection frequency reflecting the linear character of probe pulse diffraction from the transient grating. Along the excitation axis we find a significantly enhanced quadratic phase profile (figure 3(h)) compared to early waiting times T, hinting towards the nonlinear sample response mediated by TPA.

4.2. Transient shift of absorption

Figure 4(a) schematically shows the unperturbed band structure of InSb near the Γ-point with resonant TPA directly at the band gap energy. The linear absorption in InSb at 300 K (grey) in figure 4(c) is overlaid with different pulse spectra employed in the experiment. Upper and lower frequency axes are scaled with a factor two, emphasizing that optical excitation is dominated by TPA. Simultaneous attenuation of pump and probe pulse leads to a cubic power dependence of the nonlinear signal (figure 4(b)), including the quadratic power dependence of TPA and linear scaling of probe pulse diffraction. The overall nonlinear process is six-wavemixing ($\chi^{(5)}$), where the interference grating contributes a reciprocal lattice vector to achieve phase matching in the box geometry. Figure 4(d) shows the temporal evolution of vertical spectral shifts of the nonlinear signal along the excitation frequency axis at different pulse frequency (thick grey line). Red and blue arrows emphasize red- and blueshifts with respect to the source pulse frequency in the coherent regime ($T < 0.5$ ps) where pulses overlap.

Different competing processes contribute to ultrafast spectral shifts of the nonlinear signal. The increase of linear (and two-photon [37]) optical absorption towards higher frequencies (figure 4(c)) leads to higher excitation efficiency on the high-energy part of the spectrum, causing a general blueshift of the excitation at all frequencies. In contrast, resonant excitation of carriers via TPA near the onset of linear absorption (23 THz pulse frequency, green profile) leads to a significant redshift at early delay ($T < 500$ fs). The overlap of strong electric fields induces coherent effects such as optical Stark shifts [38, 39] and the Franz–Keldysh effect [40, 41], which modulate the effective bandgap. Our measurements reveal a net redshift along the excitation frequency axis, hinting towards a dominant contribution of the Franz–Keldysh effect when all fields overlap. The magnitude of this redshift depends approximately linearly on power as indicated by figure 4(d). Additional bandgap renormalization by photo-excited carriers remains a long-lived effect in the experiment, since the carrier lifetime is much longer than the investigated dynamics and the total carrier density remains low due to the nonlinear excitation.

In contrast to the investigation of phonon coherences by Somma *et al.* [8], the spectral energy of pulses in this work is fully off-resonant with respect to lattice resonances and solely probes carrier dynamics in the vicinity of the InSb absorption edge. Electric field strengths around 200 kV cm^{-1} lie in a perturbative regime owing to the nonresonant spectrum of the driving pulses with respect to the fundamental bandgap and the lack of linear absorption [6]. The amplitude of nonlinear signals obtained with InSb is three orders

of magnitude higher than the sensitivity of the setup, paving the way for the investigation of much weaker signals in functional thin-film materials and metallic systems with strong broadband absorption.

5. Conclusion

In this work, we present a novel setup for coherent two-dimensional spectroscopy in the mid infrared with complete resolution of the optical field that allows us to perform experiments with access to sub-cycle temporal resolution and to the phase of the signal. The experiments target solid state materials with peak electric fields of several hundreds of kV cm^{-1} and sufficient sensitivity to resolve nonlinear signals with amplitudes that are four orders of magnitude weaker down to few tens of V cm^{-1}. A noncollinear box geometry allows for geometric filtering of the signals in addition to conventional frequency filtering in post processing. These advantages are enabled by the sensitive detection scheme based on electro-optic samping of the nonlinear signals rather than exploiting the interference with a local oscillator. Finally, we demonstrate the capabilities of our setup by performing 2D spectroscopy on bulk InSb. A transient redshift of the nonlinear response along the excitation axis within the coherent overlap of all three interacting pulses is a dominant effect, uniquely accessible with two-dimensional spectroscopy. These results pave the way towards the study of complex low-energy and many-body phenomena in condensed matter systems as well as their correlations and dynamics on ultrafast time scales.

Data availability statement

The data that support the findings of this study are available upon reasonable request from the authors.

Acknowledgments

This project has received funding from the European Union's Horizon 2020 research and innovation programme under the Marie Sklodowska-Curie Grant Agreement No. 812992. This work was supported by the FEDER Program (Grant No. 2017-03-022-19 'Lux-Ultra-Fast'). The authors thank Professor Dr. Alfred Leitenstorfer for helpful discussions.

ORCID iDs

Thomas Deckert https://orcid.org/0000-0001-7320-7860
Jonas Allerbeck https://orcid.org/0000-0002-3912-3265
Takayuki Kurihara https://orcid.org/0000-0001-6903-002X
Daniele Brida https://orcid.org/0000-0003-2060-5480

References

[1] Hamm P and Zanni M 2011 *Concepts and Methods of 2D Infrared Spectroscopy* (Cambridge: Cambridge University Press)
[2] Mukamel S 1999 *Principles of Nonlinear Optical Spectroscopy* (New York: Oxford University Press)
[3] Reimann K, Woerner M and Elsaesser T 2021 Two-dimensional terahertz spectroscopy of condensed-phase molecular systems *J. Chem. Phys.* **154** 120901
[4] Cundiff S T and Mukamel S 2013 Optical multidimensional coherent spectroscopy *Phys. Today* **66** 44–9
[5] Kampfrath T, Tanaka K and Nelson K A 2013 Resonant and nonresonant control over matter and light by intense terahertz transients *Nat. Photon.* **7** 680–90
[6] Junginger F, Mayer B, Schmidt C, Schubert O, Mährlein S, Leitenstorfer A, Huber R and Pashkin A 2012 Nonperturbative interband response of a bulk InSb semiconductor driven off resonantly by terahertz electromagnetic few-cycle pulses *Phys. Rev. Lett.* **109** 147403
[7] Somma C, Folpini G, Reimann K, Woerner M and Elsaesser T 2016 Phase-resolved two-dimensional terahertz spectroscopy including off-resonant interactions beyond the $\chi^{(3)}$ limit *J. Chem. Phys.* **144** 184202
[8] Somma C, Folpini G, Reimann K, Woerner M and Elsaesser T 2016 Two-phonon quantum coherences in indium antimonide studied by nonlinear two-dimensional terahertz spectroscopy *Phys. Rev. Lett.* **116** 177401
[9] Runge M, Kang T, Biermann K, Reimann K, Woerner M and Elsaesser T 2021 Mono-cycle terahertz pulses from intersubband shift currents in asymmetric semiconductor quantum wells *Optica* **8** 1638–41
[10] Kuehn W, Reimann K, Woerner M, Elsaesser T and Hey R 2011 Two-dimensional terahertz correlation spectra of electronic excitations in semiconductor quantum wells *J. Phys. Chem.* B **115** 5448–55
[11] Kuehn W, Reimann K, Woerner M, Elsaesser T, Hey R and Schade U 2011 Strong correlation of electronic and lattice excitations in GaAs/AlGaAs semiconductor quantum wells revealed by two-dimensional terahertz spectroscopy *Phys. Rev. Lett.* **107** 67401
[12] Woerner M, Kuehn W, Bowlan P, Reimann K and Elsaesser T 2013 Ultrafast two-dimensional terahertz spectroscopy of elementary excitations in solids *New J. Phys.* **15** 25039

[13] Lu J, Li X, Hwang H Y, Ofori-Okai B K, Kurihara T, Suemoto T and Nelson K A 2017 Coherent two-dimensional terahertz magnetic resonance spectroscopy of collective spin waves *Phys. Rev. Lett.* **118** 207204
[14] Mahmood F, Chaudhuri D, Gopalakrishnan S, Nandkishore R and Armitage N P 2021 Observation of a marginal Fermi glass *Nat. Phys.* **17** 627–31
[15] Giannetti C 2016 New perspectives in the ultrafast spectroscopy of many-body excitations in correlated materials *Riv. Nuovo Cimento* **39** 1–10
[16] Budweg A, Yadav D, Grupp A, Leitenstorfer A, Trushin M, Pauly F and Brida D 2019 Control of excitonic absorption by thickness variation in few-layer GaSe *Phys. Rev.* B **100** 45404
[17] Novoselov K S, Mishchenko A, Carvalho A and Castro Neto A H 2016 2D materials and van der Waals heterostructures *Science* **353** aac9439
[18] Lepetit L, Chériaux G and Joffre M 1995 Linear techniques of phase measurement by femtosecond spectral interferometry for applications in spectroscopy *J. Opt. Soc. Am.* B **12** 2467–74
[19] Hochstrasser R M 2007 Two-dimensional spectroscopy at infrared and optical frequencies *Proc. Natl Acad. Sci.* **104** 14190
[20] Zheng J, Kwak K, Asbury J, Chen X, Piletic I R and Fayer M D 2005 Ultrafast dynamics of solute-solvent complexation observed at thermal equilibrium in real time *Science* **309** 1338–43
[21] Allerbeck J, Deckert T, Spitzner L and Brida D 2021 Probing free-carrier and exciton dynamics in a bulk semiconductor with two-dimensional electronic spectroscopy *Phys. Rev.* B **104** L201202
[22] Nardin G, Autry T M, Moody G, Singh R, Li H and Cundiff S T 2015 Multi-dimensional coherent optical spectroscopy of semiconductor nanostructures: collinear and non-collinear approaches *J. Appl. Phys.* **117** 112804
[23] Grupp A, Budweg A, Fischer M P, Allerbeck J, Soavi G, Leitenstorfer A and Brida D 2018 Broadly tunable ultrafast pump-probe system operating at multi-kHz repetition rate *J. Opt.* **20** 14005
[24] Jarasiunas K, Stonys S and Sirmulis E 1986 Transient gratings in InSb at two-photon excitation *IEEE J. Quantum Electron.* **22** 1341–3
[25] Miller A 1998 Transient grating studies of carrier diffusion and mobility in semiconductors *Nonlinear Optics in Semiconductors II* (*Semiconductors and Semimetals*) vol 59 ed E Garmire and A Kost (San Diego: Academic Press) pp 287–312
[26] Knoester J and Mukamel S 1991 Transient gratings, four-wave mixing and polariton effects in nonlinear optics *Phys. Rep.* **205** 1–58
[27] Allerbeck J, Deckert T, Spitzner L and Brida D 2022 Visible/multi-THz 2D spectroscopy for phase-sensitive investigation of ultrafast carrier dynamics in strongly correlated materials (in preparation)
[28] Madelung O 2004 *Semiconductors: Data Handbook* 3rd edn (Berlin: Springer)
[29] Sheik-bahaei M, Mukherjee P and Kwok H S 1986 Two-photon and three-photon absorption coefficients of InSb *J. Opt. Soc. Am.* B **3** 379
[30] Gallagher Faeder S M and Jonas D M 1999 Two-dimensional electronic correlation and relaxation spectra: theory and model calculations *J. Phys. Chem.* A **103** 10489–505
[31] Hughes S, Ciesla C M, Murdin B N, Pidgeon C R, Jaroszynski D A and Prazeres R 1995 Third-order nonlinearities and coherent transient grating effects of narrow-gap semiconductors in the midinfrared *J. Appl. Phys.* **78** 3371–5
[32] Bruhns H and Kruse H 1980 Lifetime of charge carriers in intrinsic indium antimonide *Phys. Status Solidi b* **97** 125–33
[33] Laff R A and Fan H Y 1961 Carrier lifetime in indium antimonide *Phys. Rev.* **121** 53–62
[34] Wertheim G K 1956 Carrier lifetime in indium antimonide *Phys. Rev.* **104** 662–4
[35] Zitter R N, Strauss A J and Attard A E 1959 Recombination processes in p-type indium antimonide *Phys. Rev.* **115** 266–73
[36] Avery D G and Jenkins D P 1955 XVI. Measurements of diffusion length in indium antimonide *J. Electron. Control* **1** 145–51
[37] Miller A, Johnston A, Dempsey J, Smith J, Pidgeon C R and Holah G D 1979 Two-photon absorption in InSb and $Hg_{1-x}Cd_xTe$ *J. Phys. C: Solid State Phys.* **12** 4839–49
[38] Hulin D and Joffre M 1990 Excitonic optical Stark redshift: the biexciton signature *Phys. Rev. Lett.* **65** 3425–8
[39] Binder R, Koch S W, Lindberg M, Schäfer W and Jahnke F 1991 Transient many-body effects in the semiconductor optical Stark effect: a numerical study *Phys. Rev.* B **43** 6520–9
[40] Chin A H, Bakker J M and Kono J 2000 Ultrafast electroabsorption at the transition between classical and quantum response *Phys. Rev. Lett.* **85** 3293–6
[41] Yacoby Y 1968 High-frequency Franz–Keldysh effect *Phys. Rev.* **169** 610–9
[42] Ioffe Institute 2021 InSb—indium antimonide: optical properties of InSb http://ioffe.ru/SVA/NSM/Semicond/InSb/optic.html (accessed 23 February 2021)
[43] Gobeli G W and Fan H Y 1960 Infrared absorption and valence band in indium antimonide *Phys. Rev.* **119** 613–20
[44] Johnson E J 1967 Chapter 6 absorption near the fundamental edge *Semiconductors and Semimetals* ed R K Willardson and A C Beer (New York: Academic Press) pp 153–258